High-range-resolution velocity-estimation techniques for coherent Doppler lidars with exponentially shaped laser pulses

Ljuan L. Gurdev, Tanja N. Dreischuh, and Dimitar V. Stoyanov

On the basis of an analysis of the autocovariance of the complex heterodyne signal, some novel algorithms are derived and investigated for recovering the nonuniform Doppler-velocity coherent-lidar profiles within the lidar resolution interval conditioned by the sensing laser-pulse length. The case of exponentially shaped sensing laser pulses is considered. The algorithm performance and efficiency are studied and illustrated by computer simulations (based on the use of pulse models and real laser pulses), taking into account the influence of additive noise and radial-velocity fluctuations. It is shown that, at some reasonable number of signal realizations used and with appropriate data processing to suppress the noise effects, the Doppler-velocity profiles can be determined with a considerably shorter resolution interval in comparison with that (usually accepted as a lower bound) determined by the pulse length.

OCIS codes: 280.0280, 280.3640.

1. Introduction

The range resolution of pulsed coherent Doppler lidars is usually accepted to be determined by the sensing laser-pulse length (see, e.g., Refs. 1 and 2). At the same time, the range-resolution cell and the Doppler-velocity uncertainty conditioned by the pulse length are reciprocally related, and their product is proportional to the wavelength of the laser radiation.[3] Thus a way to improve the range resolution without lowering the velocity sensitivity is to use shorter sensing pulses of shorter-wavelength laser radiation.

Another approach for improving the range resolution is to develop inverse mathematical techniques for retrieving the Doppler-velocity profiles with a considerably shorter resolution cell in comparison with the pulse length. Recently, from the analysis of the complex heterodyne signal autocovariance, we developed such techniques concerning the case of rectangular and rectangularlike pulses.[4] In the present study we take the next step by deriving and investigating some novel analogous techniques for the case of exponentially shaped laser pulses. These pulses can be good approximations of the real asymmetric laser pulses generated, e.g., by some solid-state and transversely excited atmosphere CO_2 lasers (see, e.g., Refs. 5–9). The computer simulations conducted confirm and illustrate the effective performance of the inverse techniques developed in the work.

2. Coherent Lidar Signal

The sensing radiation is considered as a sequence of quasi-monochromatic laser pulses with basic frequency ω_0, dimensionless temporal-amplitude envelope $f_0(\vartheta)$, regular (chirp) and random frequency deviations $\delta\omega_{ch}(\vartheta)$ and $\delta\omega_r(\vartheta)$, respectively, random temporal-phase fluctuations $\varphi_{or}(\vartheta)$, and a mean phase constant φ_0; ϑ is a time variable, and $f_0(\vartheta) \equiv 0$ for $\vartheta < 0$. Then the expression describing the space–time amplitude and phase distribution of the sensing laser-pulse field $\mathbf{E}_0(\mathbf{r}, t)$, at the moment t after the pulse emission, may be written in the form

$$\mathbf{E}_0(\mathbf{r}, t) = \mathcal{P}A(\mathbf{r})\, f_0(t - z/c)\exp\left\{j\left[\omega_0(t - z/c) + \int_0^{t-z/c} [\delta\omega_{ch}(t'') + \delta\omega_r(t'')]\mathrm{d}t'' + \varphi_{or}(t - z/c) + \varphi_0\right]\right\}, \quad (1)$$

where $\mathcal{P}$ is, in general, a complex vector characterizing the field-polarization state; $A(\mathbf{r})$ is a space-

L. L. Gurdev (lugurdev@ie.bas.bg), T. N. Dreischuh, and D. V. Stoyanov are with the Institute of Electronics, Bulgarian Academy of Sciences, 72 Tzarigradsko Shosse Boulevard, 1784 Sofia, Bulgaria.

Received 5 December 2000; revised manuscript received 1 October 2001.

0003-6935/02/091741-09$15.00/0

dependent factor in which, except for the aperture diffraction, the atmospheric influence (extinction, turbulence) is also taken into account (see, e.g., Ref. 10). The line of sight coincides with the axis of the pulsed laser beam. The vector coordinate $\mathbf{r}$ is expressible as $\mathbf{r} = \{\boldsymbol{\rho}, z\}$, where $\boldsymbol{\rho}$ is a transversal vector coordinate and z is a longitudinal coordinate with respect to the line of sight; $\boldsymbol{\rho} \equiv 0$ on the beam axis, and $z \equiv 0$ at the transceiver aperture plane $\{\boldsymbol{\rho}_t\} \equiv \{\boldsymbol{\rho}_t, 0\} \equiv \{\boldsymbol{\rho}, 0\}$. In the case of a linear polarization (assumed below) of the incident laser radiation, $\mathcal{P} \equiv \mathbf{e}$ is a real unit vector. The random frequency and phase fluctuations $\delta\omega_r(\vartheta)$ and $\varphi_{or}(\vartheta)$ are considered below as mutually uncorrelated stationary random processes with, respectively, mean values of $\langle \delta\omega_r \rangle = 0$ and $\langle \varphi_{or} \rangle = 0$, symmetric probability density distributions $p(\delta\omega_r) = p(-\delta\omega_r)$ and $p(\varphi_{or}) = p(-\varphi_{or})$, and autocorrelation times τ_ω and τ_φ; $\langle \, . \, \rangle$ denotes ensemble average.

Under single-scattering conditions, the field vector $\mathbf{E}_b(\boldsymbol{\rho}_t, t)$ (at the transceiver aperture plane $\{\boldsymbol{\rho}_t\} = \{\boldsymbol{\rho}_t, 0\}$, at a moment t after the pulse emission) of the radiation backscattered by aerosol particles is a superposition of elementary wave fields $\mathbf{E}_{bi}[\boldsymbol{\rho}_t, t; \mathbf{r}_i(t_i'), t']$ obtained from different scatterers having backscattering amplitudes[11] $\mathbf{a}_i$ and positions $\mathbf{r}_i(t_i')$ at the corresponding earlier moments of interaction t_i'. {The backscattered-wave propagation in the atmosphere is described by the paraxially approximated Green's function $G[\boldsymbol{\rho}_t; \mathbf{r}_i] = G_\perp[\boldsymbol{\rho}_t; \mathbf{r}_i]\exp(-j\omega_0 z_i/c)$ that takes into account in general the extinction and turbulence effects.[10]} Because of the random mutual disposition of the aerosol scatterers, the scattering process has an incoherent character; that is, the field vector $\mathbf{E}_b$ is a sum of numerous independent contributions $\mathbf{E}_{bi}$ with random amplitudes and phases. Therefore any polarization component of $\mathbf{E}_b$, such as that, for instance, corresponding to the local oscillator polarization, can be considered as a circular complex Gaussian random quantity.[12] The equivalent local-oscillator field vector $\mathbf{E}_h(\boldsymbol{\rho}_t, t)$ at the transceiver aperture plane can be given in the form $\mathbf{E}_h(\boldsymbol{\rho}_t, t) = \mathbf{A}_h(\boldsymbol{\rho}_t)\exp\{j[\omega_h t + \varphi_h(t)]\}$, where $\mathbf{A}_h(\boldsymbol{\rho}_t)$ is the spatially dependent (complex-amplitude) factor, ω_h is the optical heterodyne frequency, and $\varphi_h(t)$ is a function describing phase fluctuations.

When the photodetector collects all the local-oscillator beam energy and all the backscattered radiation that is covered by the receiving optical system, the complex photocurrent $I(t)$ resulting from coherent heterodyne detection may be represented as[13]

$$I(t) = J(t) + jQ(t) = \mathcal{K} \int \mathbf{E}_b(\boldsymbol{\rho}_t, t) \cdot \mathbf{E}_h^*(\boldsymbol{\rho}_t, t)\mathrm{d}\boldsymbol{\rho}_t, \tag{2}$$

where $\mathcal{K} = 2qe/\hbar\omega$, q is the photodetector quantum efficiency, e is the electron charge, $\hbar = h/2\pi$, h is the Planck constant, $\omega = (\omega_0 + \omega_h)/2$, and $*$ denotes complex conjugation. Functions $J(t)$ and $Q(t)$ are respectively in-phase and quadrature components of $I(t)$, which is obviously a circular complex Gaussian random quantity. Following the way described in Ref. 4, we can express the profile $I(t = 2z/c)$ of the complex signal photocurrent for pulses with an asymptotically falling tail in the form

$$\begin{aligned} I(t = 2z/c) = {} & \exp\{j[\varphi_0 - \varphi_h(t)]\} \\ & \times \sum_{l=l_1+1}^{l_2} f_0(t - 2z_l/c)\mathrm{d}\mathcal{A}(z_l)\exp\{j\omega_m(z_l)t \\ & + j\varphi_{\omega d}[(t - 2z_l/c)\chi(z_l)] \\ & + j\varphi_{or}[(t - 2z_l/c)\chi(z_l)]\}, \end{aligned} \tag{3}$$

where $z = ct/2$ is the position (along the line of sight) of the pulse front corresponding to the moment of detection t; l is the number of the aerosol slice between two adjacent (perpendicular to the line of sight) planes $\{\boldsymbol{\rho}, (l-1)\Delta z\}$ and $\{\boldsymbol{\rho}, l\Delta z\}$, Δz is an elementary step along the line of sight, $z_l = l\Delta z$, $l_1 = z_0/\Delta z$, $l_2 = ct/(2\Delta z)$, z_0 is the upper limit of the lidar dead zone (the radiation backscattered from this zone is not detectable); $\omega_m(z_l) = \omega_0\chi(z_l) - \omega_h$ is the intermediate frequency, $\chi(z_l) = 1 - 2v(z_l)/c$, $v(z_l)$ is the profile of the radial (Doppler) velocity of the aerosol scatterers; $\varphi_{\omega d}[(t - 2z_l/c)\chi(z_l)] = \varphi_{\mathrm{ch}}[(t - 2z_l/c)\chi(z_l)] + \varphi_{\omega r}[(t - 2z_l/c)\chi(z_l)]$ is the phase increment that is due to the chirp and the random frequency fluctuations, $\varphi_{\mathrm{ch}}[(t - 2z_l/c)\chi(z_l)] = \int_0^{(t-2z_l/c)\chi(z_l)} \delta\omega_{\mathrm{ch}}(t'')\mathrm{d}t''$ and $\varphi_{\omega r}[(t - 2z_l/c)\chi(z_l)] = \int_0^{(t-2z_l/c)\chi(z_l)} \delta\omega_r(t'')\mathrm{d}t''$; $\mathrm{d}\mathcal{A}(z_l) = [\Phi(z_l)\Delta z]^{1/2} w_l$ is a random differential quantity, where $w_l = w = w_r + jw_i$ is a circular complex Gaussian random quantity with zero mean value $\langle w \rangle = \langle w_r \rangle = \langle w_i \rangle = 0$ and unitary variance $Dw = \langle |w|^2 \rangle = \langle w_r^2 \rangle + \langle w_i^2 \rangle = 1$ ($\langle w_r^2 \rangle = \langle w_i^2 \rangle = \frac{1}{2}$), $\langle w_r w_j \rangle = 0$, and $\langle w_l w_{l+s} \rangle = 0$ for $s \neq 0$. Function $\Phi(z_l)$ characterizes the contribution to the mean signal power of unitary scattering length along the line of sight. Actually, according to Eq. (3), the mean signal power profile $P(t = 2z/c) = \langle |I(t - 2z/c)|^2 \rangle$ can be represented as

$$P(t = 2z/c) = \int_{z_0}^{ct/2} f(t - 2z'/c)\Phi(z')\mathrm{d}z', \tag{4}$$

where $f(\vartheta) = \langle f_0^2(\vartheta) \rangle = P_{\mathrm{imp}}(\vartheta)/P_p$ is a dimensionless shape describing the pulse power shape $P_{\mathrm{imp}}(\vartheta)$ normalized to its peak value P_p. At sufficiently short sensing pulses (physical delta pulses), Eq. (4) is reducible to the form

$$P(t = 2z/c) = P_{\mathrm{mr}}(t = 2z/c) = (c\tau_{\mathrm{eff}}/2)\Phi(ct/2), \tag{5}$$

where $P_{\mathrm{mr}}(t = 2z/c)$ is the so-called maximum resolved (short-pulse) power profile containing information about the atmospheric extinction, backscattering, turbulence etc.; $\tau_{\mathrm{eff}} = \int_0^\infty f(\vartheta)\mathrm{d}\vartheta$ is an effective pulse duration such that the total pulse energy $E_{\mathrm{imp}} = \int_0^\infty P_{\mathrm{imp}}(\vartheta)\mathrm{d}\vartheta = P_p\tau_{\mathrm{eff}}$. At known (measured) $P(t)$ and $f(\vartheta)$, the profile of $\Phi(z)$ can be recovered on the basis of Eq. (4) by use of deconvolu-

tion techniques.[14,15] An explicit expression of $d\mathcal{A}(z_l)$ is

$$d\mathcal{A}(z_l) = \mathcal{H} \sum_n \exp(-2jk_{Dl}z_{0ln}) A(\boldsymbol{\rho}_{ln}, z_l)\mathbf{a}_{nl} \cdot \int \mathbf{A}_h^*(\boldsymbol{\rho}_t) G_\perp(\boldsymbol{\rho}_t; \boldsymbol{\rho}_{ln}, z_l) d\boldsymbol{\rho}_t, \quad (6)$$

where $\boldsymbol{\rho}_{ln}$ and z_{0ln} are coordinates concerning the nth particle inside the lth slice, $\mathbf{a}_{nl}$ is the corresponding scattering amplitude, and $k_{Dl} = \omega_0\chi_l/c$; z_{0ln} is the longitudinal position of the particle when it is met by the pulse front. The slice thickness Δz may be equal to the spatial sampling interval along the line of sight that corresponds to a temporal sampling interval $\Delta t = 2\Delta z/c$. It is assumed to be large compared with the wavelength $\lambda = 2\pi c/\omega_0$, but sufficiently small that, within each slice, functions $\varphi_{\omega d}$, φ_{or}, A, $G_\perp$, and f_0 are invariable. The divergence of the pulsed laser beam (and its radius) is also assumed to be sufficiently small so that the scattering particles within each (lth) slice have uniform radial velocity $v(z_l)$, and the effect of particle motion on A and $G_\perp$ is neglected.[16,17]

3. Signal Autocovariance

The coherent lidar return signal $I(t)$ is in general a nonstationary random process. Therefore, its autocovariance $\mathrm{Cov}(t, \theta) = \langle I^*(t)I(t + \theta)\rangle$ depends not only on the time shift θ but on the moment t as well. For a positive time shift $\theta \geq 0$ (and for stable φ_h within a pulse duration), on the basis of Eq. (3) we obtain the following expression of the autocovariance function of the coherent lidar signal:

$$\mathrm{Cov}(t, \theta) = \int_{z_0}^{ct/2} dz' \langle f_0(t - 2z'/c) f_0(t + \theta - 2z'/c)\rangle \Phi(z') \exp\{j[\omega_m(z')\theta + \Delta\varphi_{\mathrm{ch}}(t, \theta, z')]\} \zeta(t, \theta, z') \xi(t, \theta, z') \times \gamma(z', 2\omega_0\theta/c), \quad (7)$$

where

$$\Delta\varphi_{\mathrm{ch}}(t, \theta, z) = \varphi_{\mathrm{ch}}[(t + \theta - 2z/c)\chi(z)] - \varphi_{\mathrm{ch}}[(t - 2z/c)\chi(z)], \quad (8a)$$

$$\zeta(t, \theta, z) = \langle \exp\{j\varphi_{\omega r}[(t + \theta - 2z/c)\chi(z)] - j\varphi_{\omega r}[(t - 2z/c)\chi(z)]\}\rangle, \quad (8b)$$

$$\xi(t, \theta, z) = \langle \exp\{j\varphi_{or}[(t + \theta - 2z/c)\chi(z)] - j\varphi_{or}[(t - 2z/c)\chi(z)]\}\rangle, \quad (8c)$$

$\chi(z) = 1 - v(z)/c$, and $\gamma(z, y) = \int \exp[-jy\tilde{v}(z)]p[\tilde{v}(z)]d\tilde{v}$ is the characteristic function corresponding to the probability density distribution $p[\tilde{v}(z)]$ of the radial-velocity fluctuations $\tilde{v}(z)$. Here we consider $v(z)$ as ensemble mean value of the radial velocity and $v_r(z) = v(z) + \tilde{v}(z)$ as a random realization of it, i.e., $\langle\tilde{v}(z)\rangle = 0$ and $\langle v_r(z)\rangle = v(z)$. For statistically isotropic (e.g., turbulent) fluctuations $\tilde{v}$, which we assume below, the probability density $p(\tilde{v})$ is a symmetric function $[p(\tilde{v}) = p(-\tilde{v})]$ leading to a real characteristic function $\gamma(z, y)$.

Let us further suppose that for time intervals T_Q of the order of θ, the phase terms φ_{ch}, $\varphi_{\omega r}$, and φ_{or} change slowly enough (τ_ω and $\tau_\varphi > T_Q$) that $\varphi(\vartheta + T_Q) - \varphi(\vartheta) \cong \varphi^I(\vartheta)T_Q$; here the superscript I denotes differentiation with respect to the variable ϑ. Then, instead of Eqs. (8a)–(8c) we can write

$$\Delta\varphi_{\mathrm{ch}}(t, \theta, z) = \varphi_{\mathrm{ch}}{}^I[(t - 2z/c)\chi(z)]\theta\chi(z) = \delta\omega_{\mathrm{ch}}[(t - 2z/c)\chi(z)]\theta\chi(z), \quad (9a)$$

$$\zeta(t, \theta, z) = \langle \exp\{j\varphi_{\omega r}{}^I[(t - 2z/c)\chi(z)]\theta\chi(z)\rangle = \langle \exp\{j\delta\omega_r[(t - 2z/c)\chi(z)]\theta\chi(z)\}\rangle, \quad (9b)$$

$$\xi(t, \theta, z) = \langle \exp\{j\varphi_{or}{}^I[(t - 2z/c)\chi(z)]\theta\chi(z)\}\rangle. \quad (9c)$$

Thus functions $\zeta(t, \theta, z)$ and $\xi(t, \theta, z)$ are represented as characteristic functions corresponding to the probability density distributions $p[\delta\omega_r(\vartheta)]$ and $p[\varphi_{or}{}^I(\vartheta)]$. The realizations of $\varphi_{or}{}^I(\vartheta)$ are derivatives of the corresponding realizations of the random function $\varphi_{or}(\vartheta)$. We assume that $\delta\omega_r(\vartheta)$ and $\varphi_{or}(\vartheta)$ are stationary zero-mean random processes with symmetric probability distributions. Respectively, $\varphi_{or}{}^I(\vartheta)$ will be also a stationary zero-mean random process with symmetric distribution $p[\varphi_{or}{}^I(\vartheta)] = p[-\varphi_{or}{}^I(\vartheta)]$. In this case functions ζ and ξ depend on only $\theta\chi(z)$ and have real values:

$$\zeta[\theta\chi(z)] = \int p(\delta\omega_r)\exp\{j\delta\omega_r\theta\chi(z)\}d\delta\omega_r, \quad (10a)$$

$$\xi[\theta\chi(z)] = \int p(\varphi_{or}{}^I)\exp\{j\varphi_{or}{}^I\theta\chi(z)\}d\varphi_{or}{}^I. \quad (10b)$$

The pulse envelope $f_0(\vartheta)$ can be represented as $f_0(\vartheta) = f_m(\vartheta)[1 + g(\vartheta)]$, where function $f_m(\vartheta) = \langle f_0(\vartheta)\rangle$ describes the mean pulse shape, and the random function $g(\vartheta) = [f_0(\vartheta) - f_m(\vartheta)]/f_0(\vartheta)$ describes the relative pulse-shape fluctuations. Then we have

$$\langle f_0(\vartheta) f_0(\vartheta + \theta)\rangle = f_m(\vartheta) f_m(\vartheta + \theta)\eta(\vartheta, \theta), \quad (10c)$$

where $\eta(\vartheta, \theta) = [1 + \mathrm{Cov}_g(\vartheta, \theta)]$ and $\mathrm{Cov}_g(\vartheta, \theta) = \langle g(\vartheta)g(\vartheta + \theta)\rangle$ is the autocovariance of $g(\vartheta)$. When the correlation time of fluctuations τ_g exceeds θ we have $\eta(\vartheta, \theta) \cong \eta(\vartheta) = [1 + \mathrm{Cov}_g(\vartheta, 0)]$, where the variance $\mathrm{Cov}_g(\vartheta, 0) = \langle g^2(\vartheta)\rangle(\ll 1)$ may depend in general on ϑ. If $\mathrm{Cov}_g(\vartheta, 0)$ is a sufficiently smooth function of ϑ, it can be replaced with some appropriate constant.

For stationary fluctuations $g(\vartheta)$, the autocovariance $\mathrm{Cov}_g(\vartheta, \theta)$ depends on only θ, i.e., $\mathrm{Cov}_g(\vartheta, \theta) \equiv \mathrm{Cov}_g(\theta)$. Then $\eta(\vartheta, \theta) \equiv \eta(\theta) = [1 + \mathrm{Cov}_g(\theta)]$. The considerations conducted below are strictly valid for

this case and for the case of absent fluctuations ($\eta = 1$).

For stationary fluctuations $g(\vartheta)$, taking into account the previous paragraph and Eqs. (9a) and (10a)–(10c), we can rewrite Eq. (7) in the form

$$\mathrm{Cov}(t, \theta) = \int_{z_0}^{ct/2} \mathrm{d}z' f_m(t - 2z'/c) f_m(t + \theta - 2z'/c)\eta(\theta)\Phi(z')\exp\{j[\omega_m(z')\theta + \delta\omega_{ch}[(t - 2z'/c)\chi(z')]\theta\chi(z')]\} \times \zeta[\theta\chi(z')]\xi[\theta\chi(z')]\gamma(z', 2\omega_0\theta/c). \quad (11)$$

$\mathrm{Cov}(t, \theta)$ is a complex function with a real part Re $\mathrm{Cov}(t, \theta) = \langle J(t)J(t + \theta)\rangle + \langle Q(t)Q(t + \theta)\rangle$ and an imaginary part Im $\mathrm{Cov}(t, \theta) = \langle J(t)Q(t + \theta)\rangle - \langle J(t + \theta)Q(t)\rangle$. At $\theta = 0$, $\mathrm{Cov}(t, \theta) = \mathrm{Cov}(t, 0)$ is equal to the mean signal power profile $P(t)$. Certainly in this case Eqs. (11) and (4) coincide.

The problem to be solved here is to determine $\omega_m(z = ct/2)$ and $v(z = ct/2)$, at known $\mathrm{Cov}(t, \theta)$ and $f_0(\vartheta)$. The possibility of solving this problem can be explained physically by the fact that, when moving along the line of sight, the sensing laser pulse involves successively new elementary slices of the scattering medium. Therefore two adjacent values of the signal, $I(t)$ and $I(t + \Delta t)$ ($\Delta t \ll \tau_{\mathrm{eff}}$), differ in the information involved about the properties of the slice between $z = ct/2$ and $z = c(t + \Delta t)/2$. This information may be extracted in principle by some differentiating procedure, but as the signal has a stochastic nature one should differentiate some statistical moments of it. To obtain the Doppler-velocity profiles, one should use statistical moments containing phase information. Such a moment is the autocovariance $\mathrm{Cov}(t, \theta)$ described mathematically (at some reasonable assumptions) by Eq. (11).

4. Retrieving the Profile of $v(z)$ with High Resolution in the Case of Exponentially Shaped Sensing Laser Pulses

We consider the mean pulse shape $f_m(\vartheta)$ in Eq. (11) as an exponentially shaped one that is given as $f_m(\vartheta) = \langle f_0(\vartheta)\rangle = (e\vartheta/\tau)\exp(-\vartheta/\tau)$, where τ is a time constant determining the pulse duration. Because $v(z) \ll c$, we can assume that the factor $\chi(z')$ in Eq. (11) is equal to unity, i.e., $\chi(z') \equiv 1$. We also assume that the frequency-chirp influence is negligible. Then we perform a three-step mathematical procedure, beginning with differentiating Eq. (11) with respect to t and performing some algebraic transformations that lead to an intermediate relation. This relation is differentiated again with respect to t, and the result is algebraically transformed anew to a second intermediate relation. As the third step, the latter relation is differentiated with respect to t, and the result obtained is reduced to the form

$$\begin{aligned}\Gamma(t, \theta) &= \mathrm{Cov}_{ttt}^{III}(t, \theta) + (6/\tau)\mathrm{Cov}_{tt}^{II}(t, \theta) \\ &\quad + (12/\tau^2)\mathrm{Cov}_t^I(t, \theta) + (8/\tau^3)\mathrm{Cov}(t, \theta) \\ &= c(e/\tau)^2 \exp(-\theta/\tau)\zeta(\theta)\xi(\theta)\eta(\theta)\psi(t, \theta) \\ &\quad \times \exp[j\omega_m(z = ct/2)\theta]\{1 + \theta/\tau \\ &\quad + \theta[\psi(t, \theta)]_t^I/[2\psi(t, \theta)] \\ &\quad + j[\omega_m(z = ct/2)]_t^I\theta^2/2\}, \end{aligned} \quad (12)$$

where $\psi(t, \theta) = \Phi(z = ct/2)\gamma(z = ct/2, 2\omega_0\theta/c)$ and the symbol ${}_t^I$ denotes differentiation with respect to t. In Eq. (12), the imaginary term in the braces can be neglected when $(\omega_m)_t^I\theta^2/2 \ll 1$. Then the following algorithm is obtained for retrieving the profile of $\omega_m(z = ct/2)$ [and respectively $v(z = ct/2)$] with a resolution cell that can be of the order of the spatial (or temporal) sampling interval Δz (or $\Delta t = 2\Delta z/c$):

$$\omega_m(z = ct/2) = \theta^{-1}\arctan[\mathrm{Im}\,\Gamma(t, \theta)/\mathrm{Re}\,\Gamma(t, \theta)]. \quad (13)$$

Inequality $(\omega_m)_t^I\theta^2/2 \ll 1$ means that the change of ω_m over each $(c\theta/2)$-long spatial interval along the line of sight should be essentially smaller than $2/\theta$, i.e., $(\omega_m)_t^I\theta = (\omega_m)_z^I c\theta/2 \ll 2/\theta$. The decrease of the value of θ leads to a proportional increase of the upper limit of the acceptable Doppler-velocity changes over $(c\theta/2)$-long intervals. Then Eq. (13) becomes applicable to Doppler-velocity profiles with sharper variations.

Another algorithm for retrieving the profile of $\omega_m(z = ct/2)$ is derived from the expression of the first derivative $G(t) = \Gamma_\theta^I(t, \theta = 0)$ of the function $\Gamma(t, \theta)$ with respect to θ at $\theta = 0$. This expression is obtained on the basis of Eq. (12) and leads to the relation

$$\omega_m(z = ct/2) = [\mathrm{Im}\,G(t)]/\{\Phi(z = ct/2) \times [ce^2\eta(0)/\tau^2]\}, \quad (14)$$

where it is taken into account that functions ξ, ζ, and γ are equal to unity when $\theta = 0$. Equation (14) represents an exact algorithm for retrieving the mean Doppler-velocity profile $v(z)$ [$\omega_m(z)$] with a resolution interval of the order of $\Delta z(\Delta t)$. This algorithm requires a preliminary experimental evaluation of the variance $\langle g^2(\vartheta)\rangle = \mathrm{Cov}_g(0)$ of the relative pulse-shape fluctuations $g(\vartheta)$ in order to determine the value of $\eta(0) = [1 + \mathrm{Cov}_g(0)]$.

5. Simulations

We simulated the algorithm performance by using various profiles of the radial Doppler velocity $v(z)$ and the mean short-pulse signal power $\propto \Phi(z)$. Below we describe and analyze for illustration the results obtained for the model of $v(z)$ shown in Fig. 1. It is a wind-vortex-like distribution of the radial velocity $v(z)$. Such a distribution is characterized by small

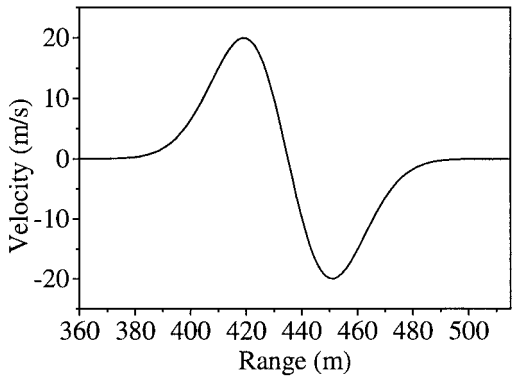

Fig. 1. Model of the wind-vortex-like distribution of the radial velocity along the line of sight.

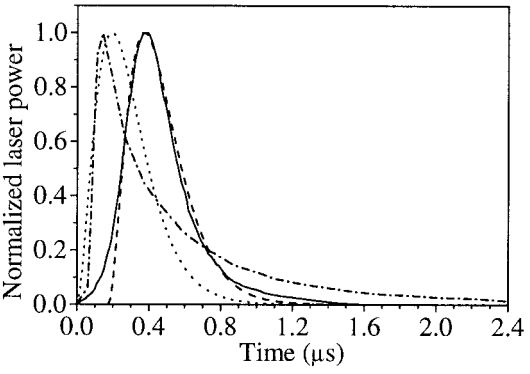

Fig. 3. Real laser-pulse shapes (dashed–dotted and solid curves) and corresponding exponentially shaped approximations (dotted and dashed curves) used in the simulations.

spatial size and sharp velocity variations.[3,18] The corresponding model of $\Phi(z)$ is shown in Fig. 2 (see also Ref. 4). The laser radiation wavelength λ, the temporal sampling interval $\Delta t = 2\Delta z/c$, and the lidar dead-zone upper limit z_0 are chosen to be $\lambda = 2$ μm, $\Delta t = 10$ ns ($\Delta z = 1.5$ m) and $z_0 = 300$ m, respectively. The pulse power shape $f(\vartheta) = f_0^2(\vartheta) = (e^2\vartheta^2/\tau^2)\exp(-2\vartheta/\tau)$ is shown in the inset of Fig. 2. We simulated the case of a stable reproducible pulse shape when $g(\vartheta) \equiv 0$. The value of τ is chosen to be 200 ns, which corresponds to an effective pulse length $l_p = c\tau_{\text{eff}} \sim 2c\tau = 120$ m. This pulse length exceeds the longitudinal wind-vortex size that is of the order of 100 m (see Fig. 1). As mentioned in Section 1, the exponential pulse waveform considered here can be a good (or even excellent[9]) approximation of various (more or less asymmetric) real laser-pulse shapes including those generated by 2-μm-wavelength solid-state lasers.[5] The aim of a prevailing part of the simulations performed is to estimate in a pure form the potentialities and the limitations of the exponential inverse algorithms derived in this paper. In this case the coherent-lidar signal and all the retrieving procedures are simulated on the basis of the pulse-shape model described above (Fig. 2). At the same time it is reasonable to estimate the quality of the exponential pulse approximations in regard to the quality of the recovered high-resolution Doppler-velocity profiles. For this purpose some simulations have been conducted in which the coherent-lidar signal synthesis and the high-resolution retrieval of the signal power profile are based on the use of real pulse shapes, and the algorithm performance is based on the corresponding exponential pulse approximations. Two authentic pulse shapes we used in simulations are given in Fig. 3 by dashed-dotted and solid curves. They are reconstructed on the basis of experimental data (concerning a 1.03-μm passively Q-switched Yb:YAG laser and a 2-μm diode-pumped Tm:YAG laser) given in Refs. 8 and 5, respectively. The corresponding exponentially shaped approximations are given by dotted and dashed curves. Let us note that it is not the case of excellent approximations. Nevertheless, as shown below, the quality of the recovered Doppler-velocity profiles is quite satisfactory. The first approximative waveform (dotted curve) closely describes the increasing part of the pulse and has nearly the same pulse-shape area; the time constant τ is 190 ns. The second approximative waveform closely describes all the pulse shape to the exclusion of some initial part of it; the time constant τ is 200 ns. The cut of the leading pulse edge (with $t_d = 170$-ns duration) corresponds to an apparent pulse-emission delay t_d that is compensated for by a shift left (equal to $z_d = ct_d/2$) of the restored radial-velocity profile.

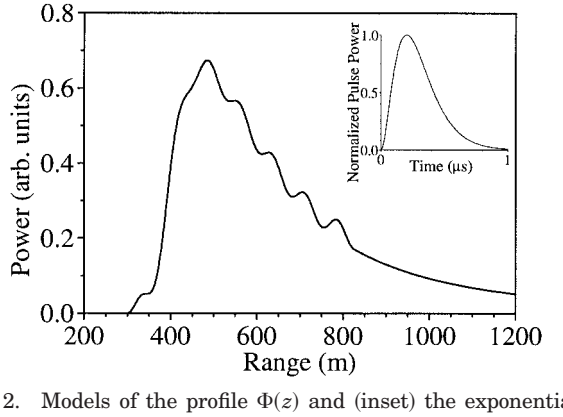

Fig. 2. Models of the profile $\Phi(z)$ and (inset) the exponentially shaped laser pulse.

The realizations of the coherent-lidar return signal $I(t) = J(t) + jQ(t)$ are simulated according to Eq. (3) (with $\varphi_h = \varphi_0 = \varphi_{\text{ch}} = 0$ and $\omega_h = \omega_0$), where the quantity $w = w_r + jw_i$ is generated as a circular complex Gaussian random variable.[4,19] Random frequency $\delta\omega_r$ and phase φ_{or} fluctuations are not especially simulated because their effect is analogous to (and can in principle be combined with) the effect of the radial-velocity fluctuations $\tilde{v}(z)$. The latter are simulated here as uncorrelated Gaussian random variables with constant standard deviation $\sigma_v(z) = \langle\tilde{v}^2(z)\rangle^{1/2} =$ constant and as normally distributed turbulent fluctuations, whose one-dimensional (along the line of sight) autocovariance is $\text{Cov}_v(\rho_z) =$

$\langle \tilde{v}(z)\tilde{v}(z + \rho_z)\rangle = 0.04C^2\epsilon^{2/3} \int_0^\infty dK \cos(K\rho_z)(K^2 + K_0^2)^{-5/6} \exp(-K^2/K_m^2)$, where $C^2 = 1.77$, ϵ is the turbulent energy-loss rate, $K_0 = 1/L_0$, L_0 is the outer turbulence scale, $K_m = 5.92/l_m$, $l_m = l_0(15C^2)^{3/4}$, and l_0 is the inner turbulence scale. The corresponding structure function $D_{zz}(\rho_z) = 2[\mathrm{Cov}_v(0) - \mathrm{Cov}_v(\rho_z)]$ is an accurate and compact approximation (over the corresponding ranges of definition) of the well-known Kolmogorov–Obukhov radial structure function.[20] For $\rho_z \gg L_0$ we obtain $D_{zz} = 2\sigma_v^2 = C^2(\epsilon L_0)^{2/3}$, i.e., $\sigma_v = C(\epsilon L_0)^{1/3}/\sqrt{2} \approx (\epsilon L_0)^{1/3}$. A similar expression for σ_v is obtainable on the basis of a more rigorous theoretical estimation.[20] Thus at constant L_0 the changes of σ_v are due to the changes of ϵ. In the simulations represented here we have assumed that $l_0 = 1$ mm, $L_0 = 100$ m, and $\sigma_v = 2$ m/s. The measuring procedure (of accumulating signal realizations) is assumed to be long enough under stationary conditions that most of the velocity variation scales can be averaged. For the case of uncorrelated velocity fluctuations the value of σ_v is assumed to be 4 m/s.

An additive stationary random noise $n(t)$ is also simulated. It can be represented as $n(t) = nw_n(t) = n[w_{nr}(t) + jw_{ni}(t)]$. In the case of uncorrelated noise, $w_n(t = l\Delta t) \equiv w_{nl} = w$ (see above), and consequently $\langle w_{nl}w_{ns}^*\rangle = 0$ for $l \neq s$. In the case of correlated noise the covariance $\mathrm{Cov}_n = \langle w_{nl}w_{ns}^*\rangle$ is chosen to have a Gaussian form $\mathrm{Cov}_n[(s - l)\Delta t] = \exp[-(s - l)^2(\Delta t)^2/\tau_n^2]$, where τ_n is the noise correlation time. Because the in-phase and quadrature channels are statistically independent, it is implied that $\langle w_{nr}w_{ni}\rangle = 0$ and $\langle w_{nr}(l\Delta t)w_{nr}(s\Delta t)\rangle = \langle w_{ni}(l\Delta t)w_{ni}(s\Delta t)\rangle = (\frac{1}{2})\exp[-(s - l)^2(\Delta t)^2/\tau_n^2]$. The signal-to-noise ratio (SNR) is specified as the ratio of the time-averaged signal power $P = [1/(t_2 - t_1)] \int_{t_1}^{t_2} P(t)dt$ to the mean noise power $P_n = n^2$; $z_1 = ct_1/2$ and $z_2 = ct_2/2$ are the initial and the final points, respectively, of the wind-vortex zone. At the same time it is clear that the actual SNR, $\mathrm{SNR}_a = P(t)/n^2$, may strongly vary with t (respectively, with z) because of strong variations of the power $P(t)$.

The covariance estimates are obtained according to the relation

$$\widehat{\mathrm{Cov}}(t, \theta = m\Delta t) = N^{-1} \sum_{k=1}^{N} [I_k(t) + n_k(t)]^*[I_k(t + m\Delta t) + n_k(t + m\Delta t)], \quad (15)$$

where $t = l\Delta t = 2l\Delta z/c$ ($l = 0, 1, 2, \ldots$), and N is the number of statistically independent (at least with respect to the additive and the speckle noise) realizations used, $I_k(t) + n_k(t)$. At $m = 0$, Eq. (15) provides the estimate $\hat{P}(t) = \widehat{\mathrm{Cov}}(t, \theta = 0)$ of the signal power profile $P(t) = \mathrm{Cov}(t, \theta = 0)$. After $\hat{P}(t)$ is known, we obtain by deconvolution[14] the estimate $\hat{\Phi}(z = ct/2)$ of the short-pulse signal power profile $\Phi(z = ct/2)$.

The simulations conducted with the above-described exponential pulse-shape model (see Fig. 2) show that algorithms (13) and (14) allow one to achieve a high spatial resolution of retrieving the profile of $v(z)$, but on the basis of sufficiently large number of realizations (laser shots) N to reduce the error that is due to noise. The corresponding data-accumulation time t_a plays the role of time constant of the measuring procedure and limits the ability of observing fast changeable atmospheric processes (whose period of stationarity $t_s < t_a$). Filtering the covariance estimate $\widehat{\mathrm{Cov}}(t, \theta)$ and the retrieved profile $v_r(z)$ [corresponding to $v(z)$], as well as $\hat{P}(t)$ and $\hat{\Phi}(z = ct/2)$, is a way to suppress the noise influence and thus to reduce the value of N required for ensuring a prescribed accuracy. However, the effective width of the filter window should have an optimum (not very large) value, ensuring a satisfactory noise suppression at an acceptable range resolution.

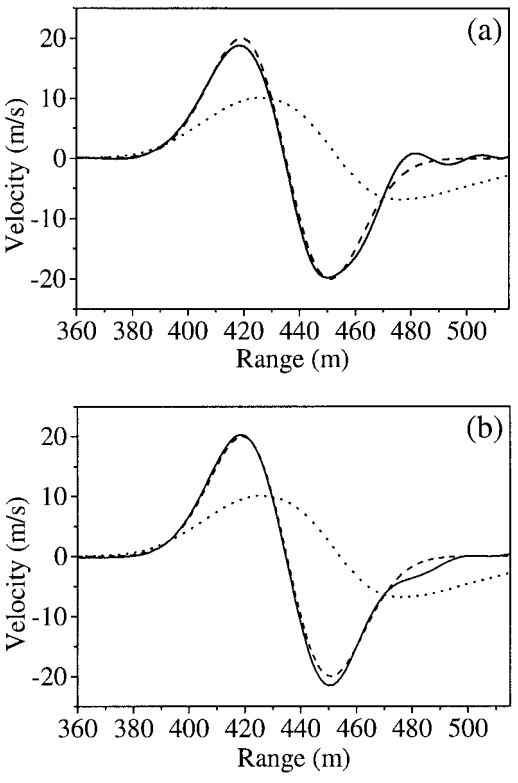

Fig. 4. Doppler-velocity profiles $v_r(z)$ restored by use of (a) algorithm (13) and (b) algorithm (14). The original profile $v(z)$ (dashed curve) and the profile resulting from applying a pulse-pair algorithm (dotted curve) are given for comparison.

Profiles of $v_r(z)$ retrieved on the basis of relations (13) and (14), in the absence of additive noise and radial-velocity fluctuations, are given by the solid curves in Figs. 4(a) and 4(b), respectively. The same results are obtained in the presence of additive noise at SNR = 100. As is evident, these profiles are closely coincident with the given (to be retrieved) wind-vortex-like model of $v(z)$ (dashed curves). The velocity deviation averaged along the line of sight (within the vortex zone) is 0.67 m/s for Fig. 4(a) and 0.54 m/s for Fig. 4(b). As everywhere in the subsequent discussion, the number of simulated signal realizations is $N = 300$, and a smoothing of $\widehat{\mathrm{Cov}}(t, \theta)$, $\widehat{\mathrm{Cov}}(t, 0)$, $\hat{\Phi}(z = ct/2)$, and $v_r(z = ct/2)$ is performed

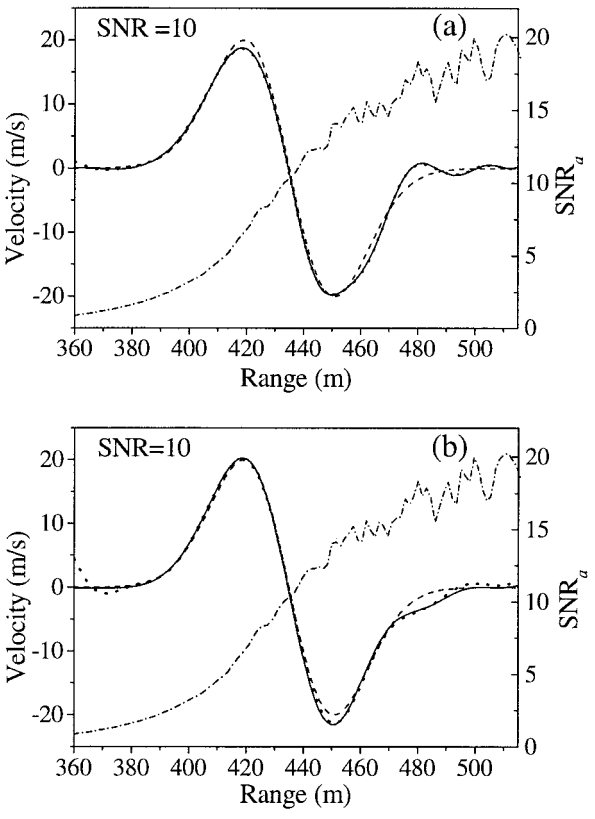

Fig. 5. Doppler-velocity profiles $v_r(z)$ (dotted curves) restored by use of (a) algorithm (13) and (b) algorithm (14) in the presence of uncorrelated additive noise. The original profile $v(z)$ (dashed curve) and the profiles restored in the absence of additive noise (solid curves) are given for comparison. The actual SNR, $\mathrm{SNR}_a(z)$, is indicated by the dashed–dotted curve.

with a smooth monotone sharp-cutoff digital filter[21] with $\pi/(10\Delta t)$-wide passband. The resolution cell achieved in this way is $R \sim 15$ m. It is less than the resolution cell $R_p = l_p/2(\sim 60$ m) that is defined by the effective pulse length $l_p \sim 120$ m.

The dotted curves in Figs. 4(a) and 4(b) represent the profile of $v_r(z)$ obtained by use of a pulse-pair (PP) algorithm.[22] The number of sampling points used along the line of sight is $M = 20$. The resolution cell achievable in this case is $R_{\mathrm{pp}} \sim 90$ m $> R_p$. The speckle noise is reduced to a negligible value by an additional averaging of $\widehat{\mathrm{Cov}}(t, \theta)$ over $N = 300$ realizations of $I(t)$. However, as is evident, there is a noticeable distortion of the restored profile $v_r(z)$ [with respect to $v(z)$] that is due to the averaging along the line of sight and to the finite pulse duration. When the number of sampling points is reduced from $M = 20$ to $M = 2$, the distortion of the profile $v_r(z)$ does not diminish as, because of the convolving effect of the sensing laser pulse, the PP resolution cell R_{pp} cannot be less than $R_p \sim 60$ m. Such a lower bound of the resolution cell is intrinsic to the Doppler-velocity estimators that do not perform any deconvolution procedures.

In Figs. 5(a) and 5(b) we have represented by dotted curves the Doppler-velocity profiles $v_r(z)$ restored by use of algorithms (13) and (14), respectively, in the presence of uncorrelated additive noise at a mean SNR = 10. The profile of the actual SNR, $\mathrm{SNR}_a(z = ct/2)$, along the line of sight is also given by a dashed–dotted curve. It is seen that there is no noticeable difference between the profiles restored in the presence of additive noise and the profiles (solid curves) restored in the absence of such a noise. As in Figs. 4(a) and 4(b), these profiles are closely coincident with the model given of $v(z)$ (dashed curve). When SNR = 1, the restored profiles $v_r(z)$ are near the model of $v(z)$ and the profiles retrieved in the absence of additive noise, but the boundary filtering effects near $z = z_0$ become more apparent.

Let us note that at uncorrelated (wideband) additive noise the statistical estimates [of $\Gamma(t, \theta)$ and $G(t)$, respectively] $\hat{\Gamma}(t, \theta) = \widehat{\mathrm{Cov}}_{ttt}^{\,III}(t, \theta) + (6/\tau)\widehat{\mathrm{Cov}}_{tt}^{\,II}(t, \theta) + (12/\tau^2)\widehat{\mathrm{Cov}}_{\,t}^{\,I}(t, \theta) + (8/\tau^3)\widehat{\mathrm{Cov}}(t, \theta)$ (at $\theta \neq 0$) and $\hat{G}(t) = \hat{\Gamma}_\theta{}'(t, \theta = 0)$ are unbiased ones, i.e., $\langle\hat{\Gamma}(t, \theta)\rangle = \Gamma(t, \theta)$ and $\langle\hat{G}(t)\rangle = G(t)$. Therefore algorithms (13) and (14) do not lead in this case to any systematic errors in the final results for $v_r(z)$. That is, at a sufficiently large statistical volume N, one can in principle recover $v(z)$ with an arbitrary high accuracy.

When the additive noise is correlated we obtain $\langle\hat{\Gamma}(t, \theta)\rangle = \Gamma(t, \theta) + \mathrm{Cov}_n(\theta)$ and $\langle\hat{G}(t)\rangle = G(t)$; $\mathrm{Cov}_n(\theta)$ is assumed to be differentiable at $\theta = 0$. Consequently, the use of algorithm (14) would not lead to the appearance of systematic errors. Such errors may arise, however, in the results obtained on the basis of Eq. (13). They are not reducible by increasing N, but can be removed if, instead of $\hat{\Gamma}(t, \theta)$, one uses in Eq. (13) another unbiased estimate of $\Gamma(t, \theta)$. Such an estimate is $\hat{\hat{\Gamma}}(t, \theta) = \hat{\Gamma}(t, \theta) - (8/\tau^3)\widehat{\mathrm{Cov}}_n(\theta)$, where $\widehat{\mathrm{Cov}}_n(\theta)$ is an experimentally determined estimate of $\mathrm{Cov}_n(\theta)$. The simulations conducted with Gaussian-correlated additive noise show that at SNR > 10 the noise influence on the final results for $v_r(z)$ is negligible. When SNR = 1, Eq. (14) leads to near results. Equation (13) leads to near results only when the estimate $\hat{\hat{\Gamma}}(t, \theta) = \hat{\Gamma}(t, \theta) - (8/\tau^3)\widehat{\mathrm{Cov}}_n(\theta)$ is used, where $\widehat{\mathrm{Cov}}_n(\theta)$ is obtained as an independent estimate of $\mathrm{Cov}_n(\theta)$ (see Fig. 6, solid curve). Then the velocity deviation averaged within the vortex zone is 1.55 m/s. When the estimate $\hat{\Gamma}(t, \theta)$ is used, the results obtained for $v_r(z)$ differ noticeably from $v(z)$ (Fig. 6, dotted curve). The correlation time τ_n has been varied in simulations from $\tau_n = 3\Delta t$ to $\tau_n = 40\Delta t$, but any visible difference has not been noted.

From the results from the simulations, one may conclude that, despite the speckle and additive noise effects, the algorithms developed here allow one to retrieve sharply varying (wind-vortex-like) Doppler-velocity profiles whose size is less than the resolution cell conditioned by the sensing laser-pulse length. The achievable average retrieving accuracy can be of the order of 1 m/s or less (at SNR ≥ 10) when appro-

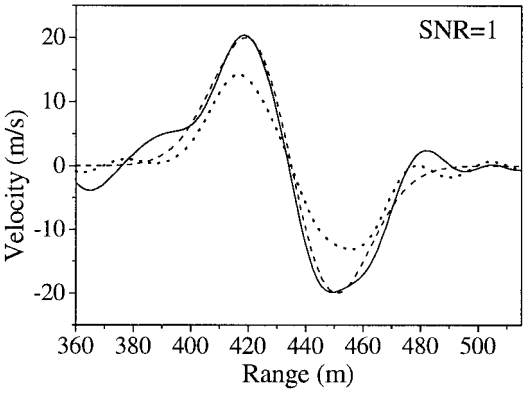

Fig. 6. Doppler velocity profiles $v_r(z)$ restored by use of algorithm (13) in the presence of correlated additive noise with (solid curve) and without (dotted curve) compensation of the bias of the autocovariance estimate. The original profile $v(z)$ (dashed curve) is also shown.

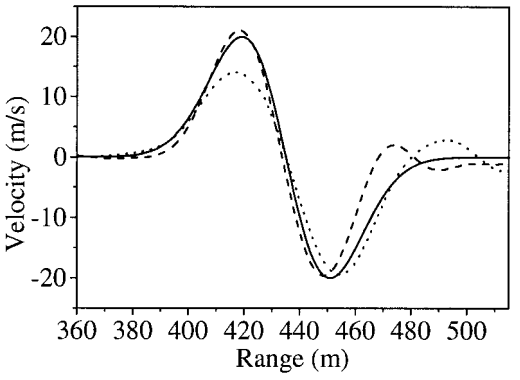

Fig. 8. Original Doppler-velocity profile (solid curve) and two profiles, restored by algorithm (14), resulting from simulations in which real laser pulses were used for synthesis of the coherent-lidar signal. The dashed and the dotted curves correspond to the dashed–dotted and the solid shapes in Fig. 3.

priate data processing is performed based on a reasonable number of signal realizations.

To show mainly the effect of the radial-velocity fluctuations, we have simulated such fluctuations in the absence of additive noise. The profiles $v_r(z)$ recovered on the basis of Eqs. (13) and (14) are shown in Figs. 7(a) and 7(b), respectively. It is seen that in the case of uncorrelated velocity fluctuations the profiles $v_r(z)$ closely follow the model $v(z)$ with rare deviations of the order of 4 m/s. The velocity deviation averaged along the line of sight (within the vortex zone) is 1.5 m/s for Fig. 7(a) and 1.56 m/s for Fig. 7(b). In the case of turbulent velocity fluctuations the profiles of $v_r(z)$ are near $v(z)$ with average deviations of 1 m/s [Fig. 7(a)] and 0.9 m/s [Fig. 7(b)] for $\sigma_v = 2$ m/s. Thus one can in principle recover $v(z)$ in the presence of relatively strong velocity fluctuations.

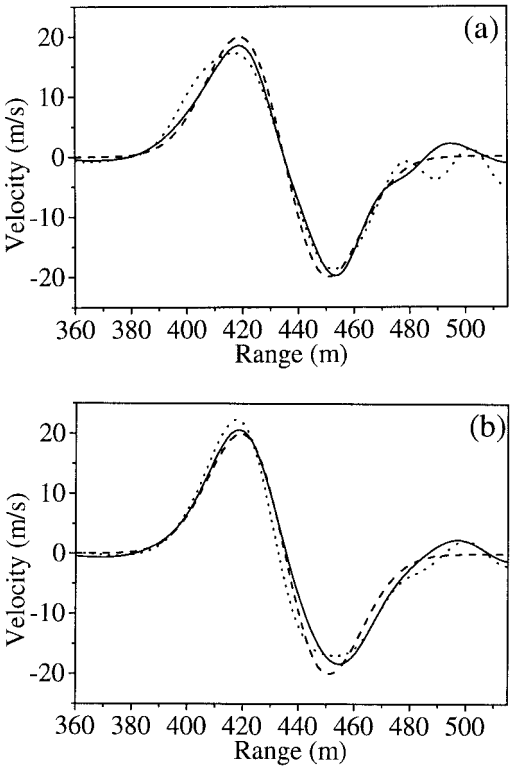

Fig. 7. Doppler-velocity profiles $v_r(z)$ recovered on the basis of (a) algorithm (13) and (b) algorithm (14) in the presence of uncorrelated velocity fluctuations with $\sigma = 4$ m/s (dotted curves) and turbulent (correlated) velocity fluctuations with $\sigma = 2$ m/s (solid curves). The original profile $v(z)$ (dashed curve) is given for comparison.

The results from simulating the performance of algorithm (14) by use of the real pulse shapes (and their exponential approximations) given in Fig. 3 are represented in Fig. 8. The results are similar to those obtained from simulating the performance of algorithm (13). It is seen that the recovered high-resolution Doppler-velocity profiles are near those obtained by simulations in which an entirely exponentially shaped pulse model is entirely used. Thus the exponential pulse-shape approximations used turn out to be suitable and effective.

6. Conclusion

In the present work we have developed inverse mathematical techniques for improving the range resolution of determining Doppler-velocity profiles on the basis of data from coherent heterodyne lidars with exponentially shaped sensing laser pulses. These techniques are based on the analysis of the complex heterodyne signal autocovariance that is represented here in a general form, taking into account the phase and frequency fluctuations of the sensing (pulsed) radiation as well as its pulse-shape fluctuations and regular frequency deviation (chirp). The fluctuations of the radial velocity of the aerosol scatterers are also taken into account.

The algorithms obtained and investigated here for retrieving high-resolution Doppler-velocity profiles are strictly valid when the chirp effect is negligible and the relative pulse-shape fluctuations are stationary. They allow one in principle to determine the Doppler-velocity profiles with an (ideal) resolution

cell that is of the order of the sampling interval. The real achievable resolution cell, however, is larger because of the filtering procedure required for suppressing the disturbing noise effects. The noise effects have been investigated by computer simulations. Except for the speckle noise that always is present, uncorrelated and correlated additive noise has also been simulated. The Doppler-velocity profile to be retrieved is chosen to have a small-size sharply varying (wind-vortex-like) form. The results from simulations show that, by using appropriate filtering procedures and bias-compensating approaches (see Section 5), one can restore satisfactorily wind-vortex-like profiles at a reasonable number of signal realizations $N = 300$. The achievable accuracy may be of the order of 1–2 m/s at a SNR of the order of unity.

The influence of the radial-velocity fluctuations has also been investigated by computer simulations. It is shown that, at a mean-square velocity deviation up to ~5 m/s, one can identify sharply varying radial-velocity distributions with an accuracy of ~1–2 m/s.

As a whole, the inverse techniques developed in this work allow one to retrieve Doppler-velocity profiles with a resolution cell that is essentially smaller than that conditioned by the pulse length.

This research was supported in part by the Bulgarian National Science Fund under grant F-907.

References

1. M. J. Post and R. E. Cupp, "Optimizing a pulsed Doppler lidar," Appl. Opt. **29,** 4145–4158 (1990).
2. R. Frehlich, S. M. Hannon, and S. W. Henderson, "Coherent Doppler lidar measurements of winds in the weak signal regime," Appl. Opt. **36,** 3491–3499 (1997).
3. S. M. Hannon and J. A. Thomson, "Aircraft wake vortex detection and measurement with pulsed solid-state coherent laser radar," J. Mod. Opt. **41,** 2175–2196 (1994).
4. L. L. Gurdev, T. N. Dreischuh, and D. V. Stoyanov, "High-resolution Doppler-velocity estimation techniques for processing of coherent heterodyne pulsed lidar data," J. Opt. Soc. Am. A **18,** 134–142 (2001).
5. T. J. Kane and J. D. Kmetec, "Diode pumped Tm:YAG laser radar transceiver," in *Coherent Laser Radar*, Vol. 19 of the 1995 OSA Technical Digest Series (Optical Society of America, Washington, D.C., 1995), pp. 285–288.
6. S. Schnell, V. Ostroumov, J. Breguet, W. Luethy, H. Weber, and I. Shcherbakov, "Acoustooptic Q switching of erbium lasers," IEEE J. Quantum Electron. **26,** 1111–1114 (1990).
7. J. Liu, D. Shen, S.-C. Tam, and Y.-L. Lam, "Modeling pulse shape of Q-switched lasers," IEEE J. Quantum Electron. **37,** 888–896 (2001).
8. J. Dong, P. Deng, Y. Liu, Y. Zhang, J. Xu, W. Chen, and X. Xie, "Passively *Q*-switched Yb:YAG laser with Cr^{4+}:YAG as the saturable absorber," Appl. Opt. **40,** 4303–4307 (2001).
9. T. Kondoh, S. Lee, D. P. Hutchinson, and R. K. Richards, "Collective Thomson scattering using a pulsed CO_2 laser in JT-60U," Rev. Sci. Instrum. **72,** 1143–1146 (2001).
10. J. Y. Wang, "Heterodyne laser radar SNR from a diffuse target containing multiple glints," Appl. Opt. **21,** 464–476 (1982).
11. A. Ishimaru, *Wave Propagation and Scattering in Random Media, Vol. 1: Single Scattering and Transport Theory* (Academic, New York, 1978).
12. J. W. Goodman, *Statistical Optics* (Wiley, New York, 1985).
13. A. E. Siegman, "The antenna properties of optical heterodyne receivers," Appl. Opt. **5,** 1588–1594 (1966).
14. L. L. Gurdev, T. N. Dreischuh, and D. V. Stoyanov, "Deconvolution techniques for improving the resolution of long-pulse lidars," J. Opt. Soc. Am. A **10,** 2296–2306 (1993).
15. L. L. Gurdev, T. N. Dreischuh, and D. V. Stoyanov, "Pulse backscattering tomography based on lidar principle," Opt. Commun. **151,** 339–352 (1998).
16. J. H. Churnside and H. T. Yura, "Speckle statistics of atmospherically backscattered laser light," Appl. Opt. **22,** 2559–2565 (1983).
17. G. M. Ancellet and R. T. Menzies, "Atmospheric correlation-time measurements and effects on coherent Doppler lidar," J. Opt. Soc. Am. A **4,** 367–373 (1987).
18. Ph. Salamitou, A. Dabas, and P. Flamant, "Simulations in the time domain for heterodyne coherent laser radar," Appl. Opt. **34,** 499–506 (1995).
19. I. N. Bronstein and K. A. Semendjajew, *Taschenbuch der Mathematik* (Nauka, Moscow, and Teubner, Leipzig, 1989).
20. V. I. Tatarski, *Wave Propagation in Turbulent Atmosphere* (Nauka, Moscow, 1967).
21. R. W. Hamming, *Digital Filters* (Prentice-Hall, Englewood Cliffs, N.J., 1983).
22. K. S. Miller and M. M. Rochwarger, "A covariance approach to spectral moment estimation," IEEE Trans. Inform. Theory **IT-18,** 588–596 (1972).